

Robust and superhydrophobic coating highly resistant to wear and efficient in water/oil separation

Oriol Rius-Ayra^{*†}, Roger Castellote-Alvarez[◇], Ana M. Escobar[‡] and Nuria LLorca-Isern[Ⓛ]

*Corresponding author: Oriol Rius-Ayra; oriolriusayra@ub.edu

[†]CMQF Departament de Ciència dels Materials i Química Física, Facultat de Química, Universitat de Barcelona, Martí i Franquès 1, 08028 Barcelona, Spain. (e-mail: oriolriusayra@ub.edu)

[◇]CMQF Departament de Ciència dels Materials i Química Física, Facultat de Química, Universitat de Barcelona, Martí i Franquès 1, 08028 Barcelona, Spain. (e-mail: rasteal7@alumnes.ub.edu)

[‡]CMQF Departament de Ciència dels Materials i Química Física, Facultat de Química, Universitat de Barcelona, Martí i Franquès 1, 08028 Barcelona, Spain. (e-mail: annaescobarromero@ub.edu)

[Ⓛ]CMQF Departament de Ciència dels Materials i Química Física, Facultat de Química, Universitat de Barcelona, Martí i Franquès 1, 08028 Barcelona, Spain. (e-mail: nullorca@ub.edu)

Abstract

Here, we report a straightforward and rapid process using fatty acids to produce a stable superhydrophobic hybrid composite coating on aluminium substrate which is highly resistant to wear under environmental conditions. Furthermore, this novel superhydrophobic metal surface is highly efficient at separating of water/oil systems. The single-step process we adopt involves electrochemical deposition of $ZnCl_2$, $\alpha-Al_2O_3$ and lauric acid ($C_{11}H_{23}COOH$) onto commercial pure aluminium substrate. The resultant static contact angle (170°) and sliding angle (1°) are those of a superhydrophobic coating with self-cleaning properties; while chemical analysis shows that this is the result of generation of zinc laurate ($Zn(C_{11}H_{20}COO)_2$) as a major compound that increases the superhydrophobic character of the coating, generating a flower-like structure 70 nm thick. Different wear tests show the coating is resistant to severe conditions, confirming its real potential against weathering, including sand and

water erosion. Finally, a water/oil separation test determined 99% separation efficiency in hexane and ether petroleum systems, in a laboratory-made storage tank.

Keywords

Superhydrobobic; Electrodeposition; Wear; Robust, Water/oil separation; composite; hierarchical structure

1. Introduction

The surface properties of superhydrophobic materials are attracting increasing attention [1,2] and they have been studied for potential applications such as self-cleaning [3], low adhesion [4], anti-smudging [5], drag-reduction [6], anti-icing [7] or anti-fogging [5]. The most useful magnitude used to classify superhydrophobic (SH) materials is the contact angle (CA) between the material surface and a water droplet; a CA greater than 150° leads to superhydrophobic behaviour, whereas a CA between 90° and 150° corresponds to hydrophobic behaviour. Superhydrophobic (also known as superwetable) systems are hierarchical structures that result from the predominant roles of micro- and nano-structural features. These combinations generate two distinct kinds of wettability states known as Wenzel (1936) [8] and Cassie-Baxter (1944) [9]; the former is defined by a homogeneous regime, while in the latter, the surface is heterogeneous and presents air pockets throughout the hierarchical structure.

Furthermore, the wettability properties of superhydrophobic surfaces can switch their wetting properties under different conditions and generate several wettability states, depending on the system [10–12]. In fact, water SH surfaces can switch to superoleophilic wettability (Fig. 1) which presents a new and innovative strategy to separate oil from water in complex systems. Different processes, chemicals and methods are reported in the literature which allows us to take advantage of this strategy. These includes materials such as cotton fabrics prepared via vapour phase deposition (PVD) of polyaniline and fluorinated alkyl silane [13]; foams modified with methyltrichlorosilane (MTCS) through a sol-gel process that permits different types of oils to be separated, such as hexane, gasoline or peanut oil [14]; meshes spray coated with corn cob powders that present underwater superoleophobicity [15]; and sponges of

polyurethane (PU) where hydroxylated nanodiamonds coated with polydopamine (PDA) react with fluorocarbons [16] and are used for separating water from oil. The capacity of different superwetable systems to switch their wettability state offers a new opportunity to apply them in different environments.

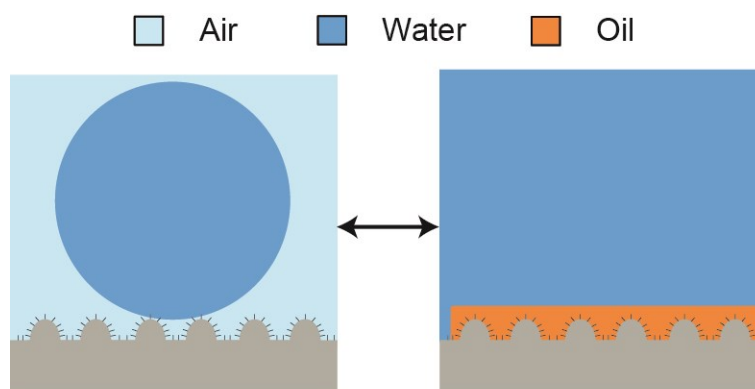


Figure 1. Two distinct superwetable systems: (left) a superhydrophobic state; (right) an underwater superoleophilic state.

A large variety of techniques and substrates [17–19] are used to prepare SH coatings, such as chemical etching [20] to generate an SH layer on aluminium substrates using lauric and hydrochloric acid as reagents; a combination of chemical etching and electrophoretic deposition [21] can also be used to obtain SH surfaces on aluminium alloys using 1H,1H,2H,2H-perfluorodecyltriethoxysilane (FAS) as a modifying agent. In electrodeposition, a single step can be used to generate an SH coating on aluminium [22] or 316L stainless steel [23,24], with lauric acid and nickel chloride. In order to enhance the properties of materials or coatings, several compounds can be selected [25]; however, ceramics play an important role in increasing resistance to chemical agents and mechanical wear. This is the case of alumina (Al_2O_3): a ceramic material used in several applications because of its excellent properties, such as chemical stability, high

degree of hardness and low cost. Some coatings are prepared using alumina which directly increases the hardness; and some electrochemical processes [26–30] also use it to increase this property, with successful results.

Herein, we report a robust superhydrophobic coating that is superoleophilic under water, possess auto-cleaning properties and it capable of separating water/oil systems in a laboratory-made separation tank to an exceptional degree. The strategy we used to produce the coating involves electrochemical deposition of zinc chloride and lauric acid onto pure aluminium substrate. The use of α -alumina particles enhanced the robustness of the coating prepared in this way. The robustness of the coated surfaces was confirmed via sandpaper abrasion, rotary slurry, high impact and blade-scratch tests. Finally, the coated aluminium substrate was used to separate two different water/oil mixtures; the separation efficiency was greater than 98% in both cases. Thus, this straightforward and rapid method produces multifunctional surfaces with great potential for practical applications in diverse fields.

2. Experimental procedure

2.1. Fabrication of superhydrophobic composite metal surfaces

The present method is used for depositing a SH coating onto pure aluminium substrate. The experimental procedure is as follows: cleaned plates of commercially pure aluminium were grounded manually and vertically with SiC abrasive paper at P1200 grade. A solution of 0.1 M lauric acid, 0.05 M ZnCl₂ and 1 g/L of α -Al₂O₃ of 0.3 μ m particle diameter (purchased from Scharlau, Acros Organics and Alfa Aesar,

respectively) was prepared in analytical grade ethanol obtaining the corresponding suspension after stirring. Two aluminium plates acting as electrodes were immersed vertically and separated 2 cm each other in the solution. Finally, a current density of 0.02 A/dm^2 was applied during different time ranges from 60 s to 1200 s. After that, the samples were removed from the electrolytic solution, cleaned with ethanol and dried in air. Samples were obtained as mentioned and the experimental conditions such as temperature ($25 \text{ }^\circ\text{C}$), reactants concentration or potential were controlled constant. A coating was formed on the aluminium substrate covering the surface. Concerning the water/oil separation experiments, deionized water as well as hexane synthesis grade and petroleum ether environmental grade (purchased from Scharlau and Alfa Aesar, respectively) were used.

2.2. Structure characterizations

In order to understand the role of reactants as well as the morphology, different characterisation techniques are used to determine morphological as well as chemical composition. Samples surface was characterised on a JEOL J-7100 scanning electron microscope (FESEM) for studying its detailed morphology, EDS microanalysis is used to determine the semiquantitative elemental composition of the generated coatings (samples were carbon sputtered to enhance observation). X-Ray Photoelectron Spectroscopy (XPS) data were operated on a PHI ESCA-5500 using a monochromatic X-Ray source ($\text{K}\alpha(\text{Al})= 1486.6 \text{ eV}$ and 350 W) to determine chemical composition of the system. Infra-red spectroscopy was also used to establish the presence of hydrocarbon acid and its chemical bonds, for this purpose a Fourier Bomem ABB FTLA (FTIR) in the range $4000\text{-}525 \text{ cm}^{-1}$ at a resolution of 4 cm^{-1} was used. X-Ray

Diffraction (XRD) was mainly used to determine the structure of the alumina powder, the equipment was a PANalytical X'Pert PRO MPD Alpha1 powder diffractometer in Bragg-Brentano $\theta/2\theta$ geometry of 240 mm of radius and Cu $K\alpha_1$ radiation ($\lambda = 1.5406 \text{ \AA}$). The roughness was measured by confocal microscopy using LeicaScan DCM3D on a surface of $1270 \times 950 \mu\text{m}^2$ and using a white light beam.

2.3. Contact angle (CA) measurements

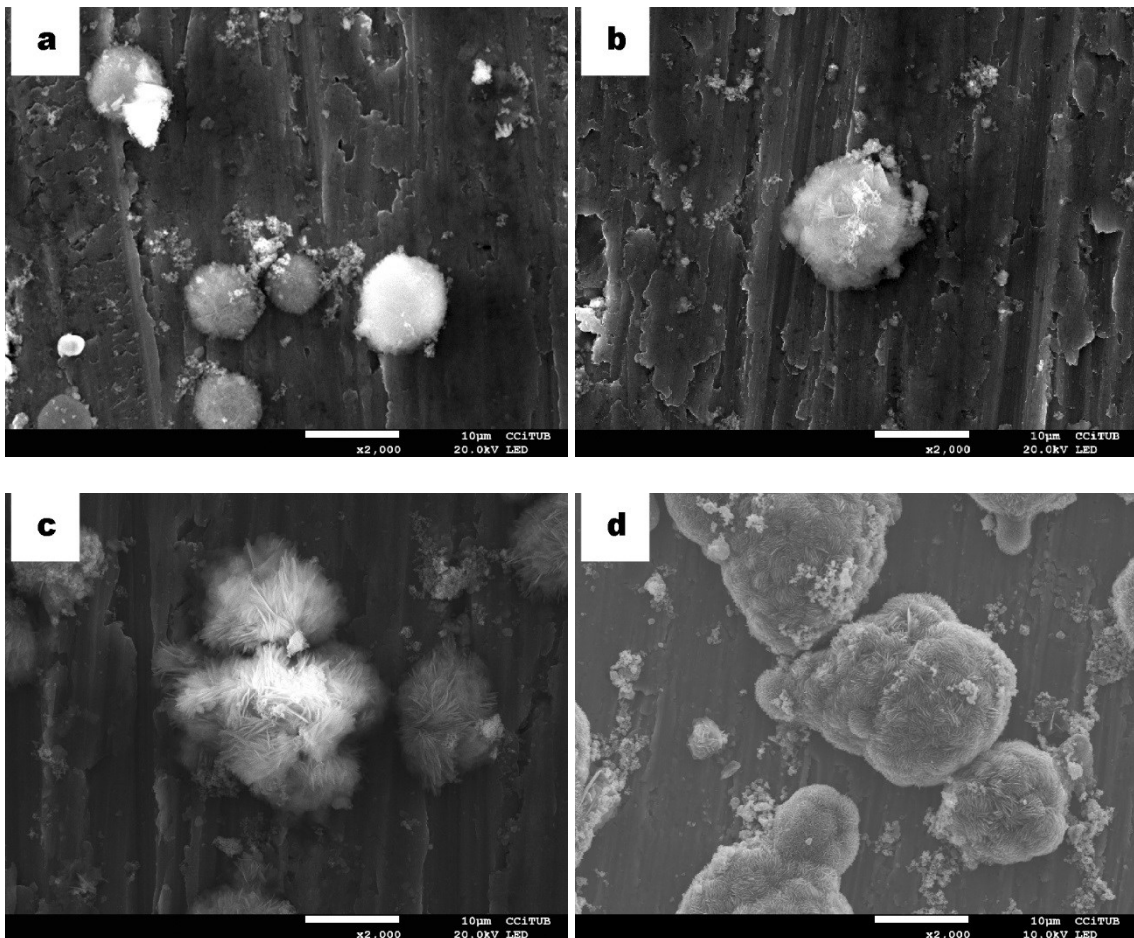
Contact angle was measured using a KRÜSS DSA 100 system (Germany) at room temperature. A drop of $10 \mu\text{L}$ ultrapure water was dropped onto the produced SH composite aluminium surfaces. The reported average CA values were obtained by three repetitive measurements of CA at different sites on the surface.

3. Results and discussion

3.1. Characterization of the superhydrophobic composite coating of aluminium surfaces

The coating surface morphology is shown in Figure 2 at different electrodeposition times. As can be seen, after 60 s and 120 s, the surface is not completely covered and the particles formed measure around $10 \mu\text{m}$ (Fig. 2 a-b); while it should be noted that $\alpha\text{-Al}_2\text{O}_3$ is perceptible in very low quantities, forming aggregates. After 300 s of electrodeposition (Fig. 2c), the particle morphology changes and they develop a randomly oriented flake shape; while $\alpha\text{-Al}_2\text{O}_3$ is found covering the particles and also

on the substrate. After 60 s, 120 s and 300 s of electrodeposition, the aluminium substrate can still be seen, as can some grinding marks left by the abrasive SiC paper. The difference becomes more noticeable after long electrodeposition times: after 900 s and 1200 s, particle morphology has changed considerably, displaying a flower-like structure. After 900 s (Fig. 2e), α -Al₂O₃ is located in the inner parts of the micro-flowers and also partially covers their surface. Finally, after 1200 s of electrodeposition (Fig. 2f), the micro-flowers are completely covered by α -Al₂O₃ crystals. As the α -Al₂O₃ particles are in suspension, they are attracted to the surface via electrophoresis [31]: charged ceramic particles move toward the surface of the cathode under the electric field.



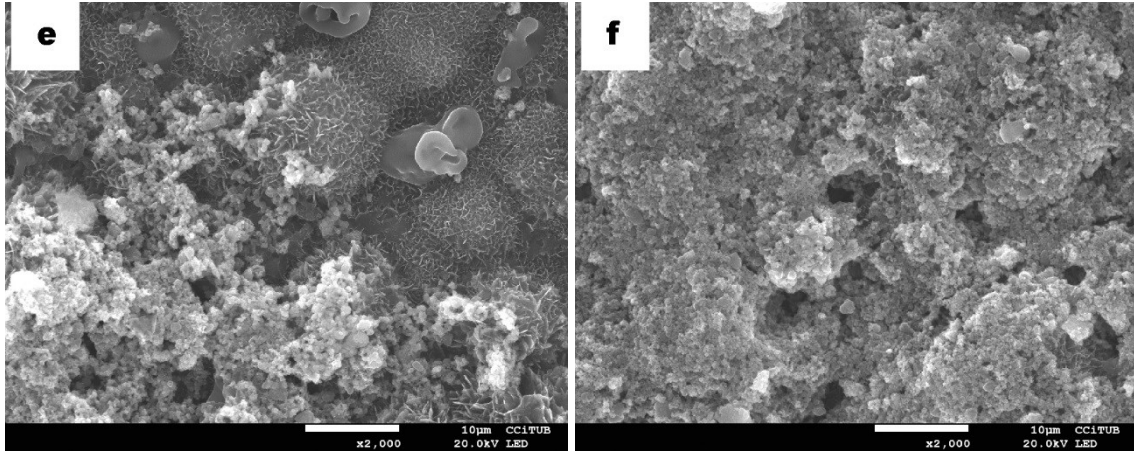


Figure 2. Representative FESEM images after electrodeposition for different times at a potential of 30 V: (a) 60 s, (b) 120 s, (c) 300 s, (d) 600 s, (e) 900 s and (f) 1200 s.

EDS microanalysis is used to determine the elemental composition of the micro-flower particles semiquantitatively, in order to establish the α -Al₂O₃ sites. As Figure 3 (left) indicates, the micro-flowers contain Zn and O; the Al signal is related to the aluminium substrate; while the high C peak is due to the carbon sputtering of the samples and the lauric acid. In the microanalysis shown in Figure 3 (right), the peaks related to Al and O are higher than in Figure 3 (left), this is due to the presence of α -Al₂O₃ in the volume analysed.

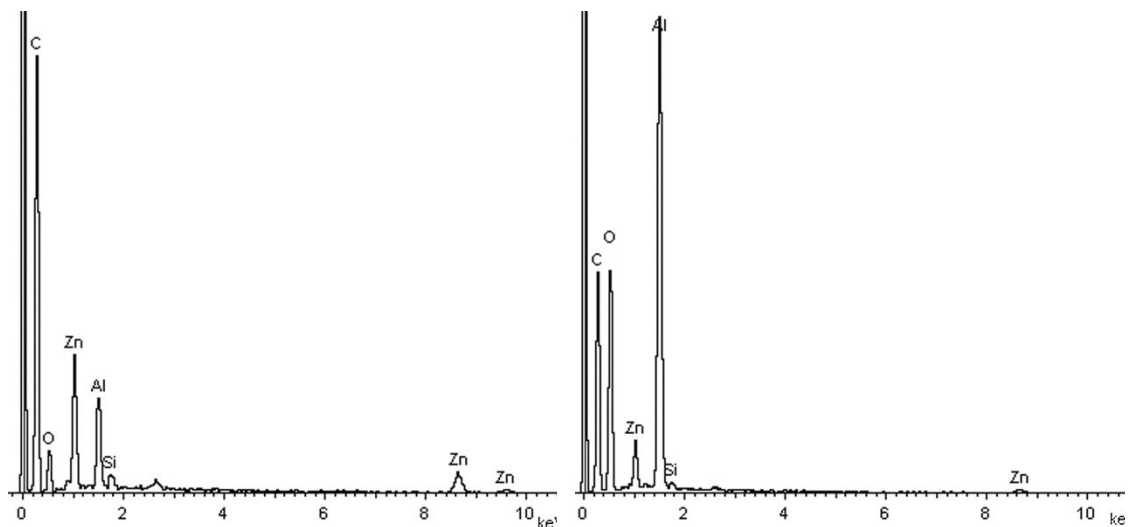


Figure 3. EDS spectra of flower-like structure at 900 s. Left: microanalysis of flower-like structure volume. Right microanalysis located at α -Al₂O₃ particles.

As the FESEM images show, initially the coating grows as islands, with no contact between them, that tend to form at grinding marks. After a certain period of electrodeposition, for example after 900 s, the initial islands has merged and formed a continuous film. This growth is typical for the Volmer-Weber mode.

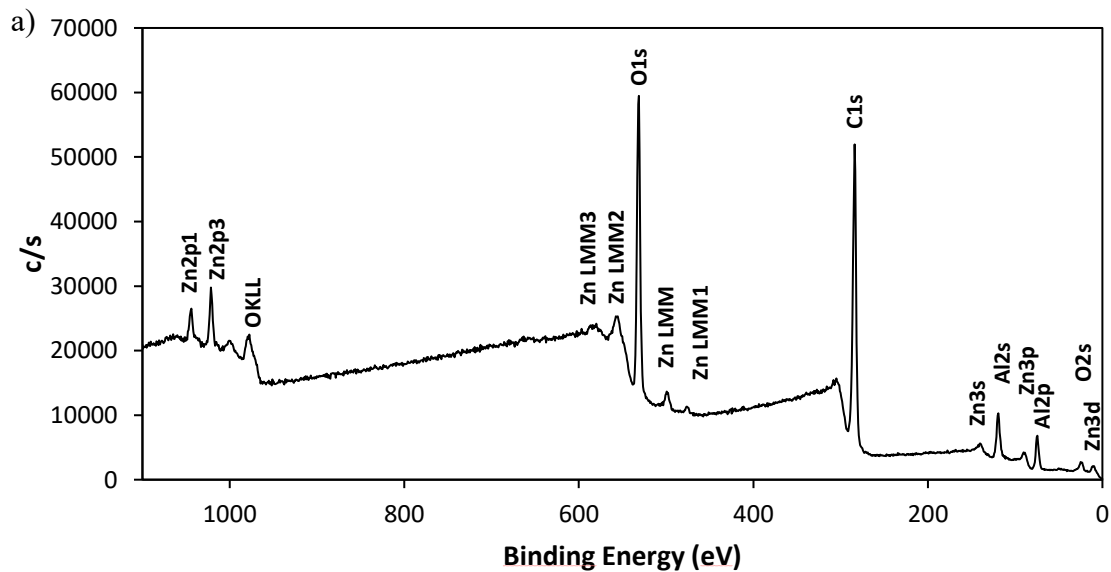
Finally, it is important to note the morphology of these structures, which are like micro-flowers, with deposited alumina maintaining its rounded morphology but generating aggregates between the “petals” and covering the flower itself. The whole micro-flower diameter reaches approximately 14 μ m. Moreover, the thickness of the petals is around 70 nm, corresponding to the nanostructured contribution to the system.

The wettability of the coating obtained is determined by measuring the static CA of the aluminium substrate and after 900 s of electrodeposition. The water CA of the aluminium substrate is 83°, thus it is considered to be hydrophilic (CA < 90°). The static water CA increases with electrodeposition time and reaches a maximum of 170° after 900 s, indicating that the surface with the micro-flower structure presents superhydrophobicity (CA > 150°). The sliding angle is also measured in order to determinate the self-cleaning properties of SH coatings. The sliding angle after 900 s of electrodeposition is 1° and since it is significantly lower than 10°, it can be considered to have self-cleaning properties, as we also demonstrated experimentally.

FESEM reveals the presence of the coating which increases the roughness of the substrate. The flower-like structure with petals provides many gaps between the petals that trap air within the hierarchical structure of the coating, which is defined as a Cassie-Baxter state. This, results in large contact angle ($CA = 170^\circ$) and small sliding angle ($SA = 1^\circ$).

3.2. Chemical characterisation

Figure 4 (a-d) shows the HR-XPS analysis of the aluminium surface after electrodeposition of the SH coating. The XPS spectrum shown in figure 4a reveals the presence of Al, C, O and Zn on the sample surface by the O-1s, C-1s, Al-2p and Zn-2p3 signals. It is important to determine the oxidation state of Zn and its relationship to lauric acid. Due to the samples were charged considerably, a neutraliser was used in order to compensate the charge of the surface.



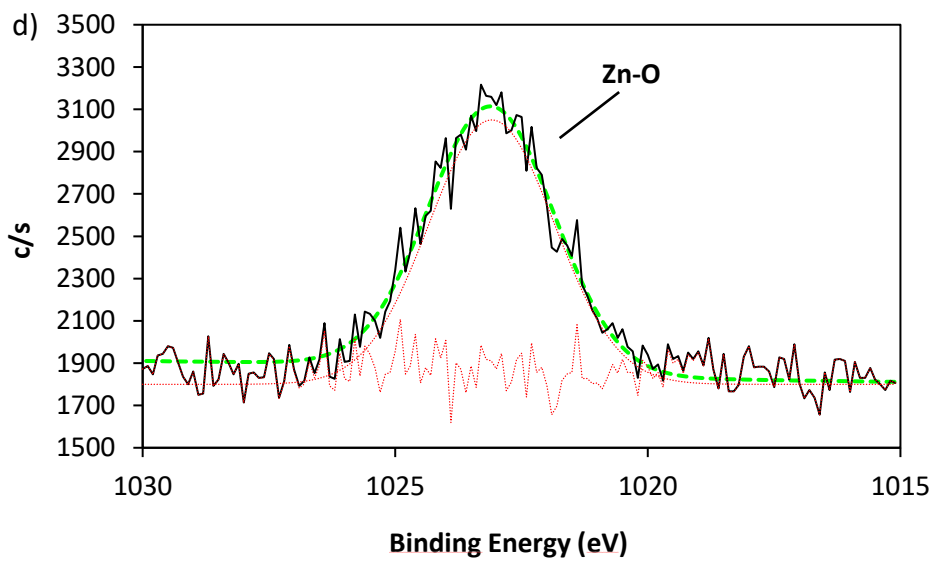
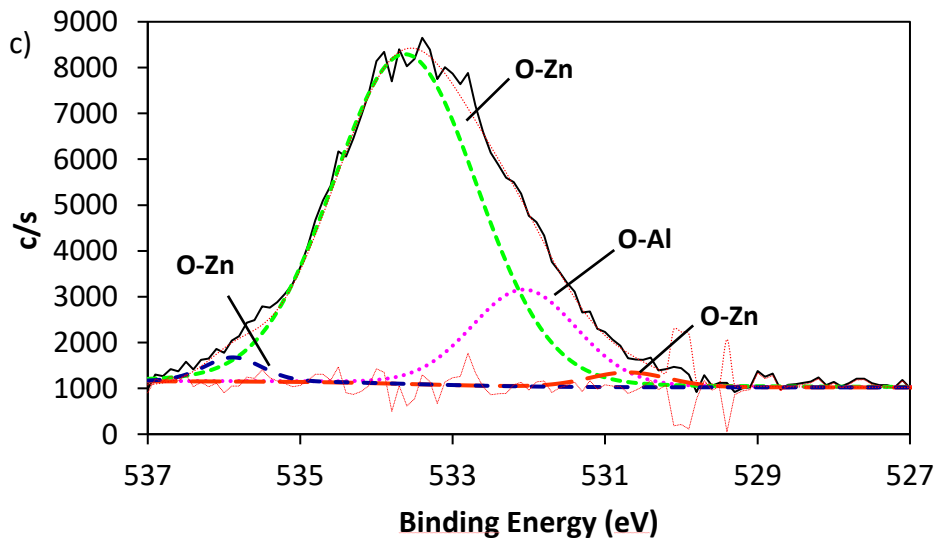
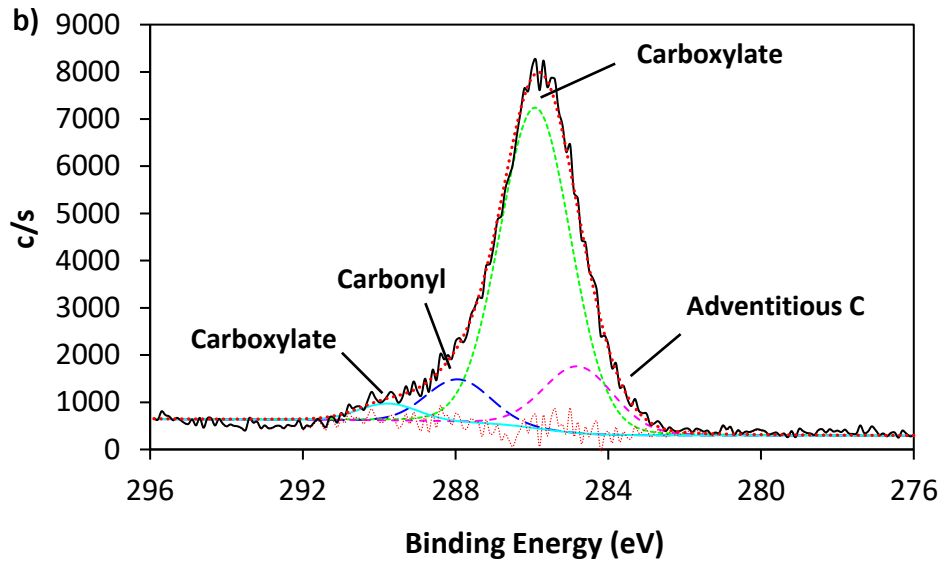


Figure 4. (a) Characteristic XPS spectra of the analysed coating and peaks from carbon, oxygen, aluminium and zinc; HR-XPS from (b) C-1s indicates carboxylate formation; (c) from O-1s is present Zn-O bond from hydroxyl and (c) from Zn-2p related to Zn²⁺ chemical state.

The HR-XPS C-1s [23,32] located at 286 eV is analysed (Table 1, Fig. 4b). Its deconvolution allows to identify the carboxylate group from the lower to the higher oxidation state of carbon by assigning four different peaks at 284 eV, 286 eV, 288 eV and 289 eV related to C-C bond, C-O bond from the carboxylate group, carbonyl group (C=O) and carboxylate group (O-C=O) respectively. Aluminium Al-2p peak [33] appears at 74 eV (Table 1) and its deconvolution generates three different peaks at 73 eV, 74 eV and 75 eV related to Al atoms in substrate, interfacial Al₂O₃ and emission of alumina surface layer. It is also detected a deconvoluted peak that appears at 76 eV and is associated to Al-O bond of alumina. From the high resolution spectrum, O-1s is found at 531 eV [34,35] (Table 1, Fig. 4c), whose deconvolution generates four peaks at 529 eV assigned to O-Zn bond from ZnO, 530 eV to O-Al assigned to α -Al₂O₃. At 531 eV and at 532 eV both deconvolutions are assigned to O-Zn bond which is related to the carboxylate (Zn(O-C=O)₂). The presence of zinc is assigned from the Zn-2p³ peak [34] (Table 1), a doublet is observed whose binding energies are at 1022 eV and a less intense due to Zn-2p₁ at 1045 eV due to the spin orbit of 23 eV. Deconvolution of the main peak gives a signal at 1022 eV that can be related to the bonding of Zn-O from the Zn(OH)₂ which is assigned to the formation of zinc carboxylate Zn(O-C=O)₂ (Fig. 4d). These results from HR-XPS prove the presence of Al₂O₃ and zinc laurate (Zn(C₁₁H₂₀COO)₂).

Table 1. Deconvolution from Al-2p, C-1s, O-1s and Zn-2p₃ in High-Resolution XPS.

Atom	χ^2	Binding Energy (eV)	Compound
Al-2p	1.773	73	Aluminium atoms in substrate
		74	Interfacial Al ₂ O ₃
		75	Emission of Al ₂ O ₃ surface
		76	Al-O bond from Al ₂ O ₃
C-1s	1.834	284	C-C bond
		286	Carboxylate group (C-O)
		288	Carbonyl group (C=O)
		289	Carboxylate group (O-C=O)
O-1s	1.154	529	O-Zn bond (ZnO)
		530	O-Al bond (α -Al ₂ O ₃)
		531	O-Zn bond (Zn(O-C=O) ₂)
		532	O-Zn bond (Zn(O-C=O) ₂)
Zn-2p ₃	1.188	1022	Zn(OH) ₂

Figure 5 shows the Fourier transform infrared spectra (FTIR) of both the produced coating and the lauric acid in order to determine their chemical composition and bonding. Different symbols are used to identify vibrations; in this case δ is used for bending, σ for rocking, ν for stretching and finally τ for twisting. Pure lauric acid [36–39] is characterized, the most characteristic bands are related to carboxyl group or carbon chain. It is important to notice the presence of a broad band between 3000-2500 cm^{-1} assigned to the carboxyl group of lauric acid. In the carbonyl group, a band at *ca.* 1689 cm^{-1} is assigned to $\nu\text{C=O}$ and at *ca.* 1298 cm^{-1} is assigned to $\nu\text{C-O}$. For carbon chain, bands appearing at *ca.* 2951 cm^{-1} , *ca.* 2911 cm^{-1} and *ca.* 2845 cm^{-1} correspond to

alkyl chain stretching and are assigned to $\nu_{\text{as}}\text{CH}_3$, $\nu_{\text{as}}\text{CH}_2$ and $\nu_{\text{s}}\text{CH}_2\text{-CH}_2$, respectively. Band located at *ca.* 1298 cm^{-1} is related to $\nu\text{O-H}$ as well as *ca.* 1192 cm^{-1} also corresponding to $\nu\text{O-H}$. A band found at *ca.* 1082 cm^{-1} is associated to σCH_3 . Two different bands found below 1000 cm^{-1} are identified in *ca.* 934 cm^{-1} and are assigned to $\delta\text{O-H}$. Finally, *ca.* 776 cm^{-1} corresponds to $\delta\text{C-H}$ out of plane.

The FTIR spectrum of the coating bands is highly similar to that of pure lauric acid [36][38–41]. However, the absence of the broad band at 3000-2500 cm^{-1} is significant and leads us to conclude that the formation of a new bond due to the carboxylic group did not occur. On the other hand, there are three strong bands, as in lauric acid spectrum, located at *ca.* 2951 cm^{-1} , *ca.* 2914 cm^{-1} and *ca.* 2846 cm^{-1} assigned to $\nu_{\text{as}}\text{CH}_3$, $\nu_{\text{as}}\text{CH}_2$ and $\nu_{\text{s}}\text{CH}_2\text{-CH}_2$, respectively. A weak band at *ca.* 1584 cm^{-1} is attributed to $\nu_{\text{as}}\text{COO}$, at *ca.* 1533 cm^{-1} , moreover, a strong band is located and is associated to $\nu_{\text{as}}\text{COO}$ and *ca.* 1400 cm^{-1} is present as a medium intense band from $\nu_{\text{s}}\text{COO}$. Strong band at *ca.* 1455 cm^{-1} is attributed to δCH_2 . Medium band *ca.* 1081 cm^{-1} is related to τCH_3 and *ca.* 716 cm^{-1} is assigned to δCH_2 .

An important difference between SH coating sample spectrum and lauric acid spectrum is the presence of broad bands with low transmittance located at *ca.* 3460 cm^{-1} assigned to $-\text{OH}$ and H-O-H bonds [42]. At low wavenumber, three bands of medium intensity at *ca.* 717 cm^{-1} , *ca.* 632 cm^{-1} and, *ca.* 572 cm^{-1} are referred to pseudoboehmite structure ($\text{AlO}(\text{OH})$).

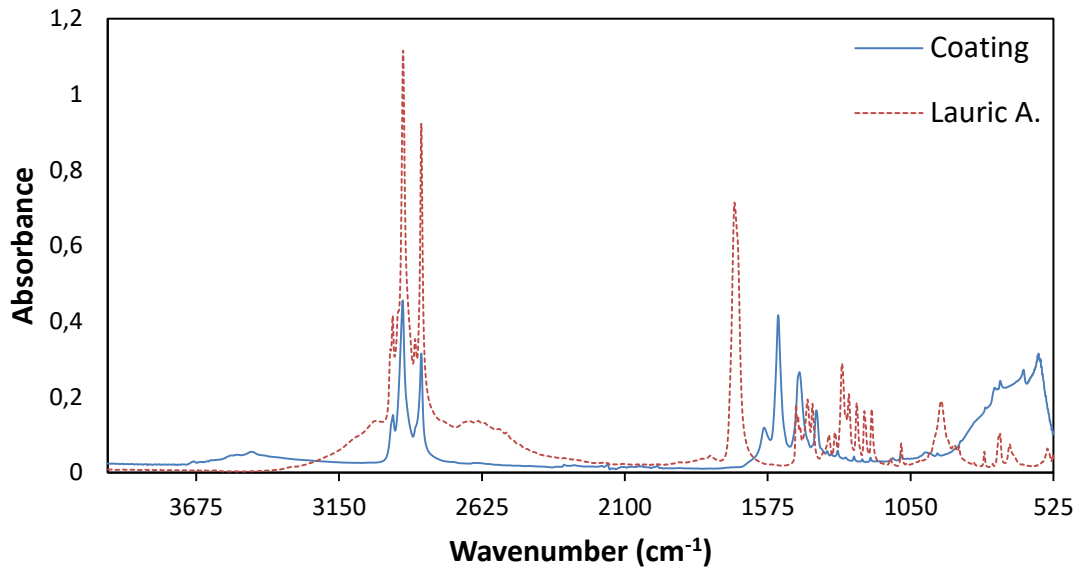


Figure 5. FTIR spectra of lauric acid and the obtained coating indicates the generation of a new carboxylate bond at ca. 1536 cm^{-1} .

Chemical characterisation techniques allowed us to identify zinc laurate ($\text{Zn}(\text{C}_{11}\text{H}_{20}\text{COO})_2$) as a product of the electrodeposition process, and this substance contributes to decreasing the surface tension of the coating. Therefore, the combination of the hierarchical structure, which increases the roughness, and the decrease in surface tension endows the coating with superhydrophobic properties.

4. Wear characterisation

To determine the wear resistance of the SH coating [43–48], we used two different severe tests under humid and dry conditions. On one hand, a rotary slurry test at different revolutions per minute (rpm) was carried out with 10 g/L of alumina particles ($140 \pm 70\ \mu\text{m}$) in water. The system consisted of a sample holder connected to a rotating

motor by a steel rod; the distance between the rotation axis and the central part of the sample was 15 mm. The samples were introduced into the slurry container for a period varying from 300 s to 1800 s, after which they were washed with ethanol and dried in air. Then, the water CA was measured for three replicates and we clearly observed that the CA decreased slightly under both test conditions. In fact, at 500 rpm and 700 rpm, the CA decreased linearly from 170° before the erosion test to 163° and 154° respectively, after 1800 s, as shown in Figure 6. As expected, the difference between the final CA values indicates that the erosion test at 700 rpm is more severe than at 500 rpm and produces greater damage to the coating surface. In case of sliding angle, in both cases it increases its value but remains lower than 10° what indicates that the coating present self-cleaning properties.

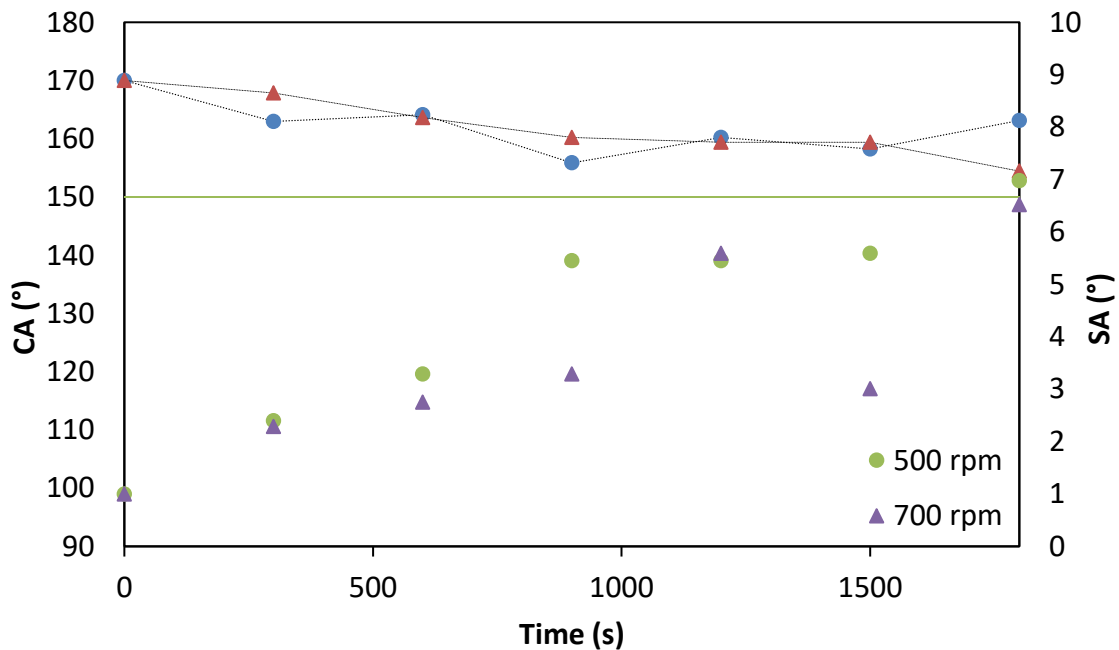


Figure 6. At different slurry test rotational velocities, the contact angle of the coating decreases but it remains superhydrophobic as it is greater than 150°. In contrast, the sliding angle (SA) increases but the surface still present anti-sticky properties.

After the rotary slurry test at both 500 and 700 rpm for 1800 s, the samples were observed by FESEM to characterise their morphology after the erosion of alumina particles (Fig. 7). As can be seen, the 500 rpm samples were unchanged with the superficial alumina particles of 0.3 μm still adhered to it. Also, the flower-like structure was still displayed all over the sample. In contrast, samples exposed to 700 rpm showed a clear morphological modification: the surface structure has suffered much more damage and is clearly smoother, compared to the flower-like structure before the erosion test.

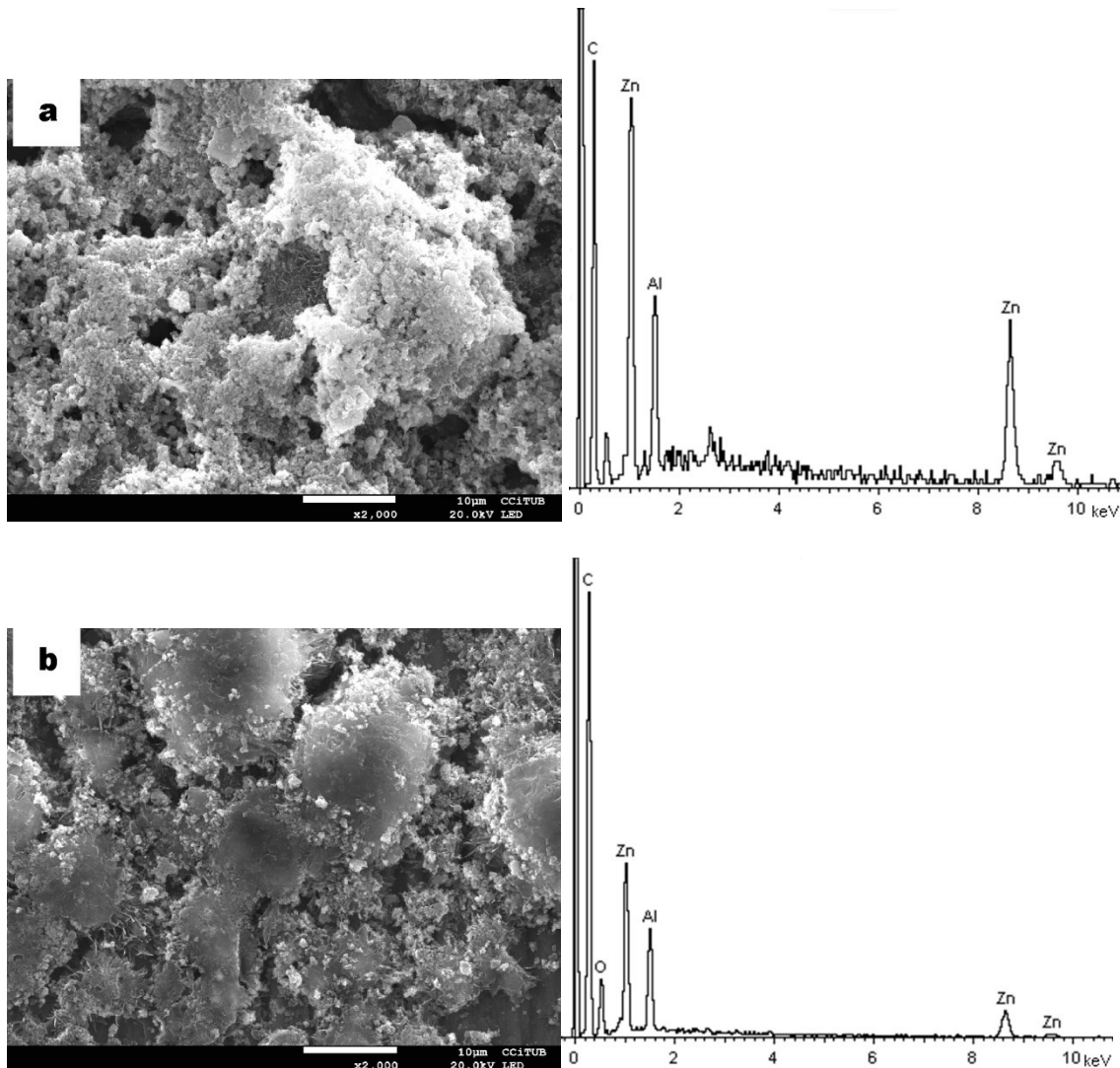


Figure 7. FESEM images and corresponding EDS after 1800 s in the slurry water abrasion test at: (a) 500 rpm and (b) 700 rpm. Images show that the slurry rotary test damaged the coating surface at the higher rotational speed, while at the lower speed the coating remained unchanged.

On the other hand, a solid particle impact test is commonly used to evaluate coating robustness; in the present study, the SH coating was impacted from various heights, with the alumina particles previously described. The sample was tilted at 45° to produce more severe erosion condition and at the same time to avoid particle accumulation. As shown in Figure 8, the water CA decreased slightly as the impact height increased, as a consequence of the damage suffered by the coating after impact, damage was more severe at 40 cm than at 10 cm. However, the SH property of the coating was maintained after alumina particle impact, as the water CA remained over 150° (CA = 159° at 40 cm impact height). *The sliding angle slightly increases at the first impact at 10 cm but remains plateau after the following impacts.*

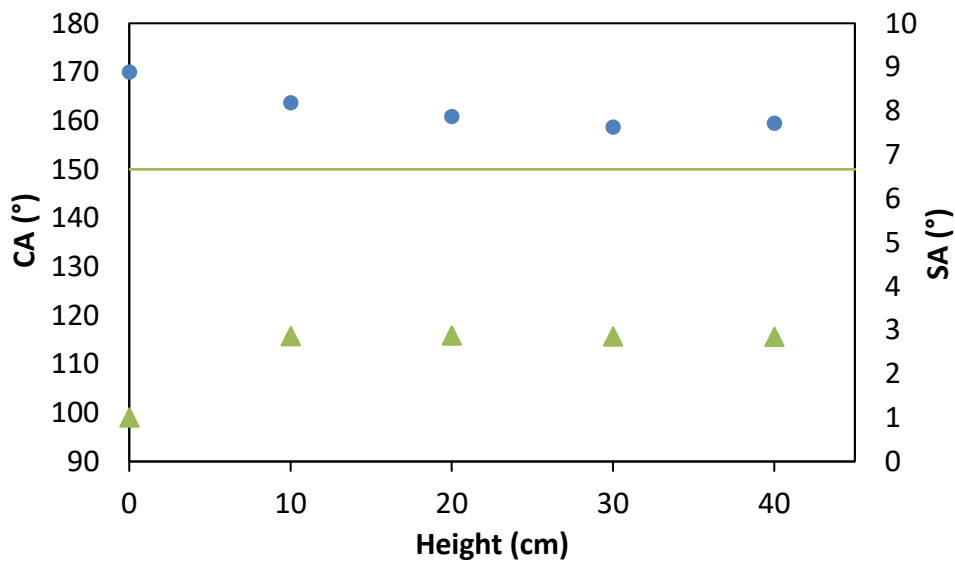


Figure 8. The contact angle decreases as the impact height increases while the sliding angle slightly increases but remains plateau.

Considering the results of the solid particle impact test at different heights and specifically at the highest value, the morphology of the sample was evaluated using FESEM.

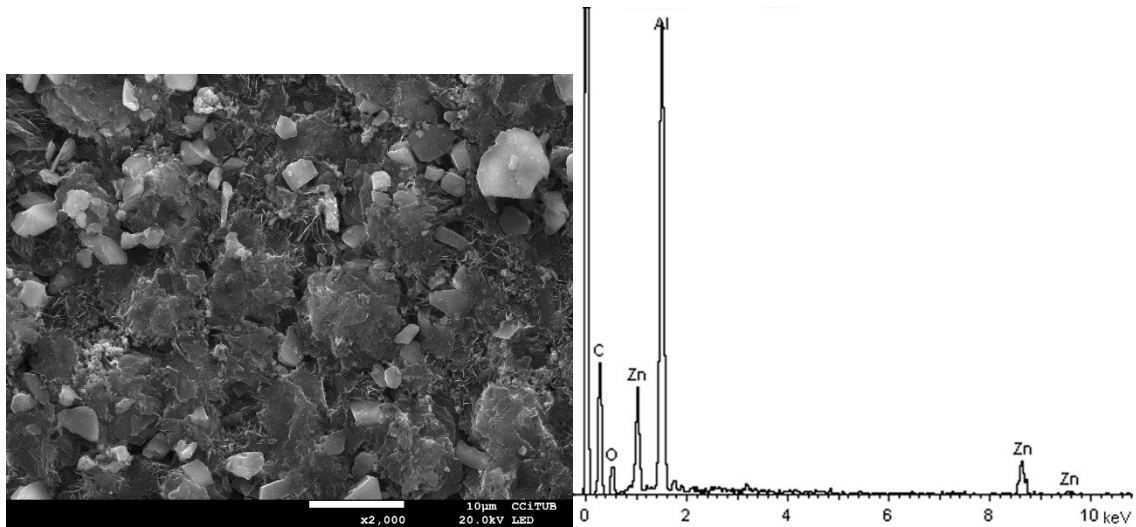
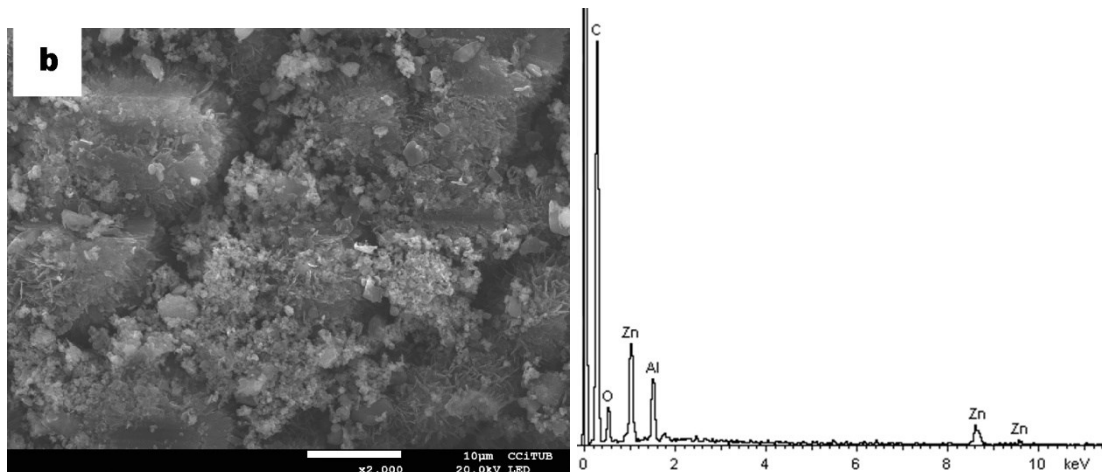
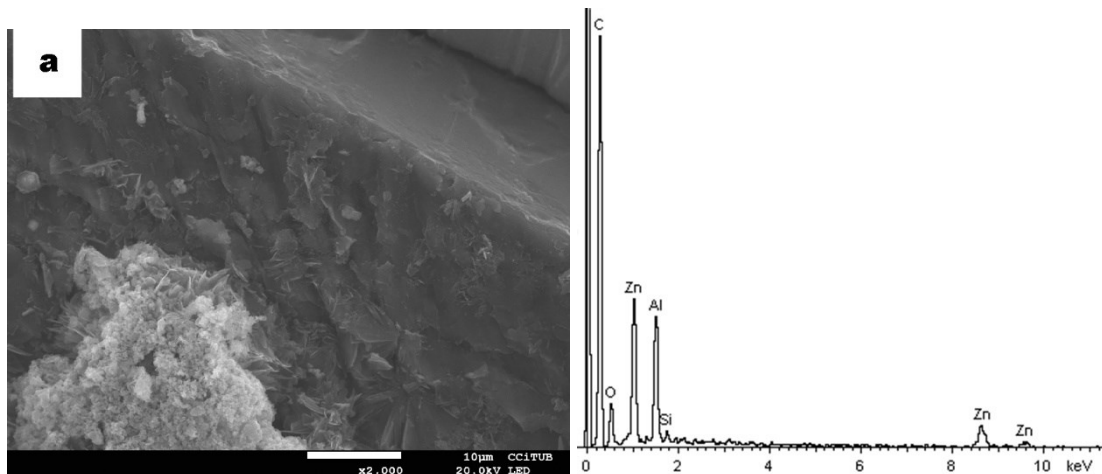


Figure 9. FESEM micrograph and its EDS of composite SH coating after the impact test (40 cm height); flower-like structure is partially damaged. Alumina from the impact test is the white particles upper right.

As Figure 9 shows, the SH coating clearly suffered damage, as the flower-like structure obtained after 900 s electrodeposition has changed. In fact, the initial morphology remains in some areas but in general the entire surface is damaged due to the severe impact of the alumina particles, which are also visible over the entire surface. The EDS spectrum shows the presence of Zn, C, O and Al, with the last of these showing the most intense peak. This is assigned to the presence of alumina on the substrate as a result of the impact test, as well as from the pure aluminium substrate.

To complete the wear characterisation and evaluate the mechanical robustness of the as-prepared SH surface, the blade-scratch and sandpaper abrasion tests were also performed. A blade was used to scratch the electrodeposited coating and thus examine the surface robustness. The coating retained its SH ($CA = 169^\circ$) and self-cleaning properties ($SA = 2^\circ$) after the test, despite the blade scratching the aluminium substrate (Fig. 10a). Meanwhile, the sandpaper abrasion test is an effective method to evaluate the resistance to mechanical abrasion of SH surfaces (Fig. 10 b-c). Here, the sandpaper abrasion test was carried out using P1200 SiC sandpaper as the abrasive surface. The SH coating was placed in contact with the sandpaper and a weight of 15 g or 30 gr was placed on it before it was moved 10 cm across the sand paper.



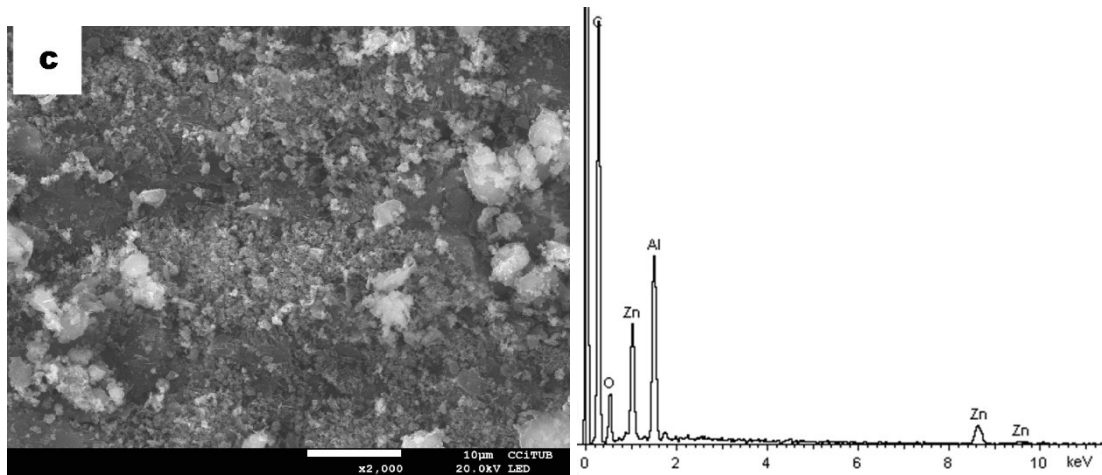


Figure 10. FESEM micrograph after abrasion test: (a) blade test; (b) abrasion test (15 g) and (c) abrasion test (30 g).

The water CAs after the test were 150° and 165° respectively, which indicated that the SH properties were retained, even after 10 sandpaper abrasion cycles (Fig. 11).

Moreover, as the sliding angle is a key parameter in determining the robustness of the coating, after the sandpaper test, the sliding angle was affected and its value increased, but as it remained below 10° , the coating maintained its self-cleaning properties. After the first cycle of the abrasion test, alumina powder could be found on the sandpaper.

Despite this powder, after subsequent cycles, the surface was still SH. As it can be seen in Figure 10 a-c, the EDS presents peaks assigned to Zn, Al or O, which are the main constituents of the SH coating; thus, this reveals that the first layer of alumina particles is removed without greatly affecting the wettability properties of the coating.

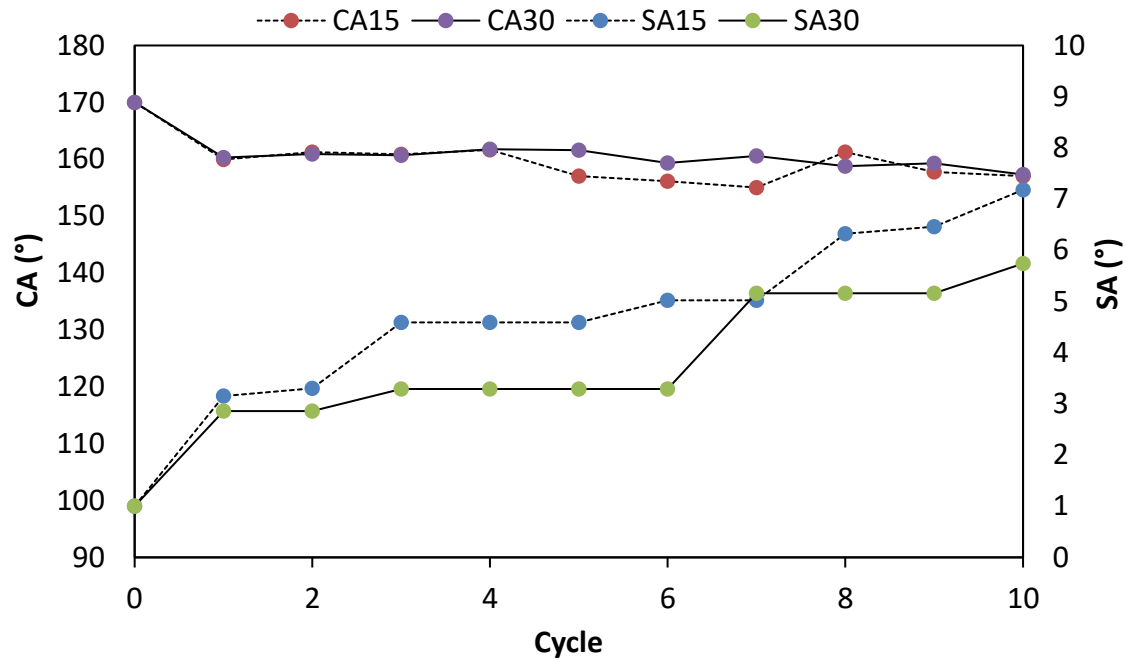


Figure 11. The superhydrophobic coating was scratched in the sandpaper abrasion test although after 1.00 m of abrasion it was still SH (CA) and also present self-cleaning properties (SA).

The root mean square (RMS) roughness was measured to analyse the SH behaviour before and after the abrasion tests (Table 2).

Table 2. RMS measurements after wear characterisation tests

Test	Unscratched	Rotary slurry test		Impact test	Scratch test		
Sample	SH coating	500 rpm	700 rpm	40 cm	15 g	30 g	Blade
RMS (μm)	3.86	4.16	1.07	4,37	1.22	1.19	10.3
CA ($^{\circ}$)	170	163	154	159	157	157	169
SA ($^{\circ}$)	1	7	6	3	7	6	2

In the case of the rotary slurry test, the difference between the two values is due to the test at 700 rpm being more severe and capable of smoothing the surface to some extent, although the roughness was still notable with CA = 154°. In contrast, at 500 rpm, the RMS value = 4.16 μm : higher than for the unscratched sample, which must be because

some α -alumina is removed from the surface. It is particularly notable that even after the high speed erosion test the coating still maintained its SH properties, which also indicates good compaction of α -alumina particles. The solid particle impact test presented an RMS value = 4.37 μm at a height of 40 cm; and the wettability properties were not excessively affected. Roughness values after the sandpaper abrasion test were similar, but in the case of the 30 g weight, the value was less than for the 15 g weight, which indicates that the weight affects performance in the scratch test and the surface is modified without loss of superhydrophobicity. The blade-scratch test provided the highest RMS roughness values, as it was the most severe test used. Despite this, the CA and sliding angle were only slightly modified; thus, the coating also presented superwettability properties.

Even though the roughness was affected by the durability test as well as by the abrasion test, the SH properties remained as the CA was greater than 150° . The sliding angle was also less than 10° , so the coating maintained its anti-adherent properties. In general terms, the severe tests produced a decrease of approximately 2.6 μm in the RMS roughness values, which indicates a smoothing of the surface. Where the RMS roughness value is higher than for the unscratched sample, as in case of 700 rpm slurry and the 40 cm impact tests, some α -alumina particles were removed, but the layers below remained unaffected; this combination increased the roughness while the surface SH was maintained. These results show that α -alumina particles, which are well known as a hard material, play an important role in the robustness of the SH coating, enhancing its capacity to endure under severe conditions.

5. Water/oil separation

The wettability of SH surfaces may switch to superoleophilic under water conditions. In this particular case, a laboratory-made SH tank for water/oil separation was designed with high surface roughness. Different volumes (ranging from 1 mL to 4 mL) of two distinct oils, hexane and petroleum ether, were used and the volume of water was maintained constant at 6 mL. During the process, time and separation rate (ξ) as well as separation efficiency (η) were studied. The separation efficiency is defined in Eq. 1.

$$\eta = m/m_0 \cdot 100 \quad (\text{Eq. 1})$$

where m_0 is the water mass before the separation and m the water mass after the process. The hexane and petroleum ether separation results reveal high values of efficiency: 98.4% and 99.7% respectively. These values prove that the process is extremely useful for water/oil separation and provides elevated of pure water recuperation. In addition, the separation rate (ξ) defined by Eq. 2 is also studied

$$\xi = S/V \cdot t \quad (\text{Eq. 2})$$

where S is the coating surface, V is the volume of oil and t is the time of separation process.

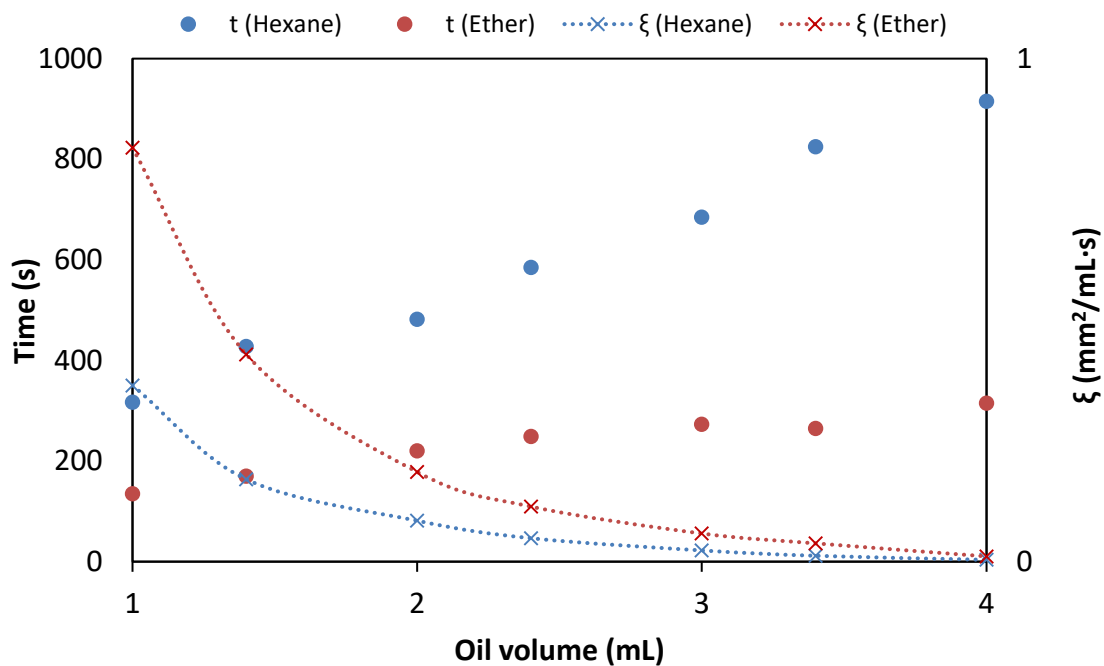


Figure 12. The water/oil separation time increases, as the volume of oil increases, while the separation rate (ξ) decreases exponentially.

Figure 12 shows the separation time against volume of oil. As can be seen, the separation time increases linearly in both petroleum ether and hexane. Meanwhile ξ decreases exponentially in both organic solvents; this indicates that as the oil volume increases, the surface of the SH tank decreases, which leads to a reduction of separation capacity.

In order to characterize the stability of the coating under different solvents, the samples were immersed in 20 mL of: water, ethanol, acetone, hexane and petroleum ether, under stirring for 120 s (Fig. 13).

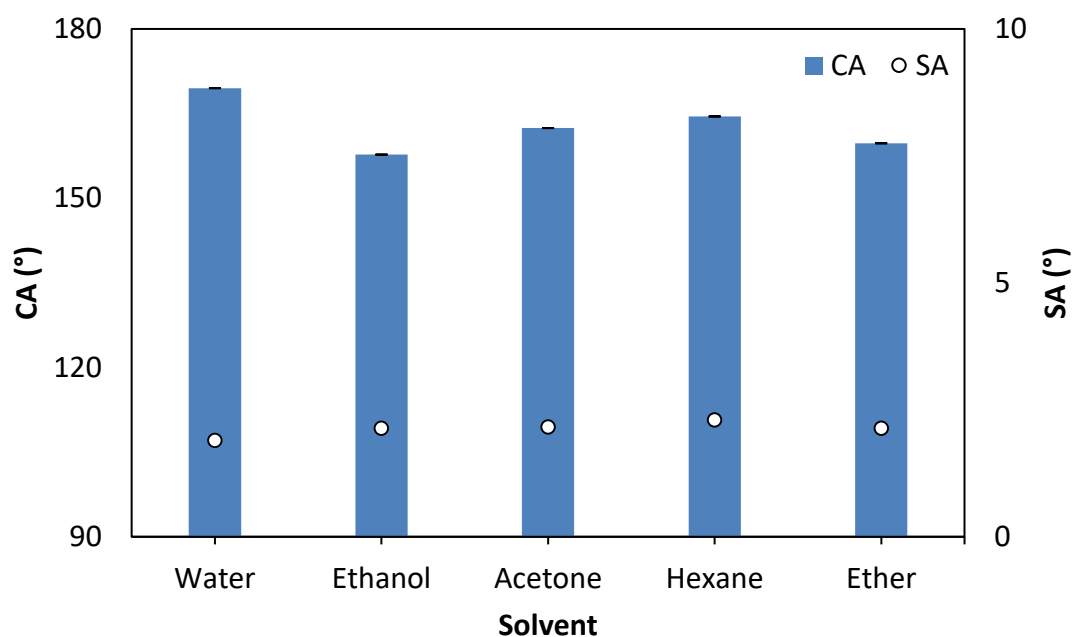


Figure 13. After solvent immersion with stirring, the wettability properties were almost not affected.

After the exposure to water, the CA was not modified and remained at 170°; this shows the capacity of laurate to repel water: its hydrophobic properties. After the exposure of the coating to different organic solvents (Fig. 13), the CA decreased only slightly and the coating still remained SH. Meanwhile, in all cases the sliding angle remained unmodified and the coating continued to presents self-cleaning properties. Considering the solubility of the organic solvents, which in the case of ethanol and acetone are miscible in water, but hexane and petroleum ether are not, we established that the laboratory-made tank was useful for the latter two solvents. Moreover, because ethanol and acetone are miscible with hexane and ether, it is possible to clean the tank after water/oil separation without loss of SH or superoleophilic properties under water systems. In this particular case, we were able to assess the capacity of the laboratory-made SH tank to repeat the process after several cycles, and determine the recyclability

of the system after exposure to hexane and petroleum ether. After 16 cycles of water/oil separation, the coating was not greatly affected by the organic solvents, thus allowing us to repeat the process without loss of SH properties.

In order to study the behaviour of the laboratory-made SH tank, once immiscible solvents were separated, a water/oil emulsion [49–53] was prepared under constant stirring, 30 mL of deionized water was emulsified with 1 mL of hexane and 0.15 g of Tween 80 as a well-known emulsifier. After the emulsion was stabilized, the SH coating was used to separate the water/oil system.

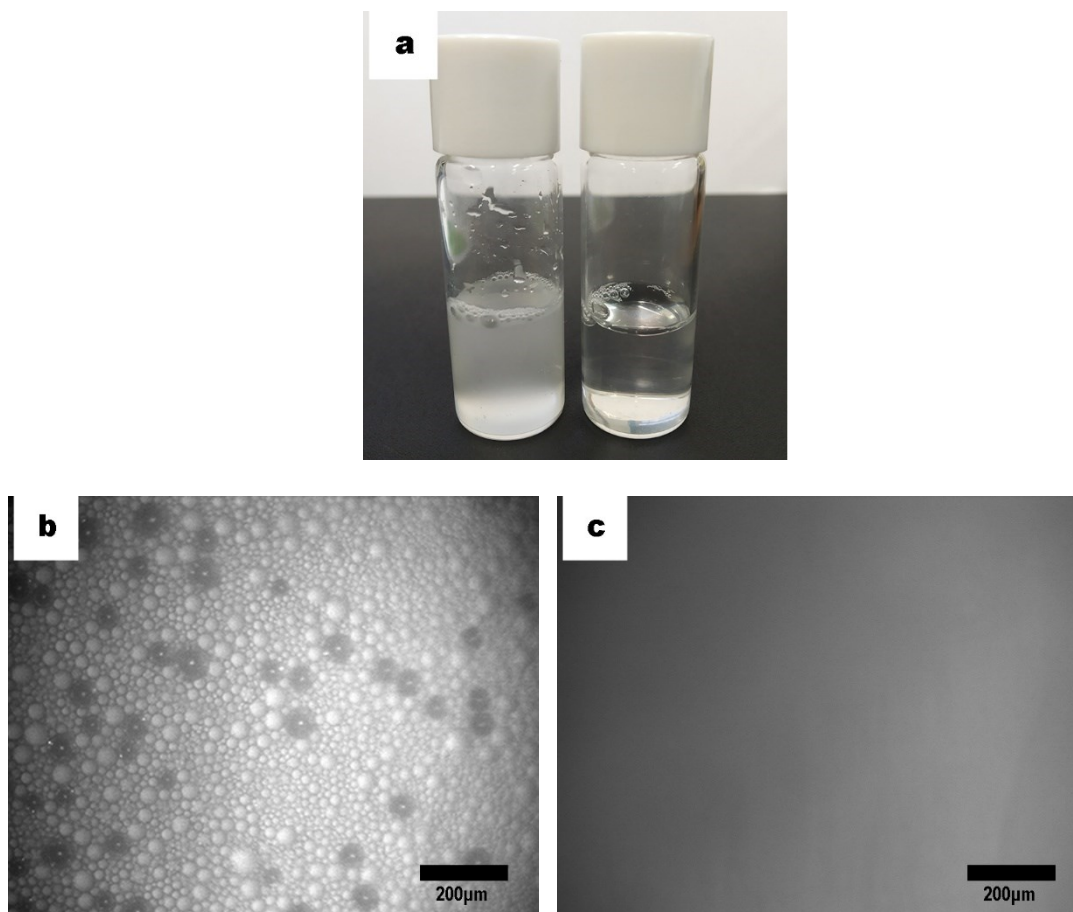


Figure 14. Water/hexane emulsion prepared to be separated in the laboratory-made tank, (a) (left vial) the emulsion is clearly separated and no hexane is present (right vial); Optical microscopy image before (b) and after (c) the separation.

As shown in Fig. 14a, the as-prepared hexane-in-water emulsions were poured into a glass tube. Once in contact with the SH coating, stabilized emulsion droplets were demulsified and the hexane phase was separated through the SH surface. Droplet size range experiments varied from 15 μm to 70 μm (as the emulsion depends on their size: increased droplet size causes the decreased stability of an emulsion), larger droplet size distribution was calculated using 200 droplets for the smaller range and 50 droplets for the larger ones. The efficiency of the separation was the same for all the range. The collected solution was clearly transparent, different from the original milk-like solution. It can be seen that after the oil separation, only water phase is observable in order that the bulk behaviour of the emulsions is proved. The optical microscopy images of emulsions before (Fig. 14b) and after the separation (Fig. 14c) proved that the oil from the stabilized emulsions was removed successfully with separation yield = 89% (Eq. 1). Because of that, figure 14c is unfocused due to water phase is the only observed system and evidences the lack of significant residual oil in the liquid phase. This test allows water/oil emulsions, which are complex system, to be separated.

The water/oil separation test in a laboratory-made SH tank permits different water/oil mixtures and emulsions to be separated due to the superoleophilic properties of the SH coating under water conditions. Moreover, the coating is not greatly affected by the organic solvents and its SH properties are not lost. This characteristic water/oil separation property opens up new options for water purification using robust superhydrophobic materials.

6. Conclusions

A new composite coating with SH properties, based on zinc chloride, lauric acid and α -alumina particles of sub-micron size, was obtained on an aluminium substrate. The static CA and sliding angle were measured with excellent results (CA: 170° , and sliding angle: 1°) demonstrating its self-cleaning properties.

The detailed structure of the coating is flower-like, with alumina particles (α - Al_2O_3) adhered between layers (*petals* of the flower-like structure). Zinc laurate ($\text{Zn}(\text{C}_{11}\text{H}_{20}\text{COO})_2$) provides the grafting system, and is combined with α - Al_2O_3 to form the constituents of the coating.

This new SH coating system resists severe damage in a rotary slurry test, solid particle impact test, sandpaper test and blade test which are useful methods to simulate environmental and aggressive conditions. This approach confirms the great potential of the SH composite coating and opens up a new concept in outdoor applications.

A water/oil separation process was also evaluated and the pure water separation efficiency (η) was high. In addition, the separation rate (ξ) show the dependence of the process on the SH surface, which plays a key role in the water/oil separation. Moreover, the tank present high recyclability after sever test under different organic solvents.

7. Funding sources

This research did not receive any specific grant from funding agencies in the public, commercial, or not-for-profit sectors.

8. References

- [1] B. Bhushan, Y.C. Jung, Natural and biomimetic artificial surfaces for superhydrophobicity, self-cleaning, low adhesion, and drag reduction, *Prog. Mater. Sci.* 56 (2011) 1–108. doi:10.1016/j.pmatsci.2010.04.003.
- [2] G.D. Bixler, B. Bhushan, Rice and butterfly wing effect inspired low drag and antifouling surfaces: A review, *Crit. Rev. Solid State Mater. Sci.* 40 (2015) 1–37. doi:10.1080/10408436.2014.917368.
- [3] B. Zhang, Y. Li, B. Hou, One-step electrodeposition fabrication of a superhydrophobic surface on an aluminum substrate with enhanced self-cleaning and anticorrosion properties, *RSC Adv.* 5 (2015) 100000–100010. doi:10.1039/C5RA21525K.
- [4] G.S. Watson, D.W. Green, B.W. Cribb, C.L. Brown, C.R. Meritt, M.J. Tobin, J. Vongsvivut, M. Sun, A.P.

- Liang, J.A. Watson, Insect Analogue to the Lotus Leaf: A Planthopper Wing Membrane Incorporating a Low-Adhesion, Nonwetting, Superhydrophobic, Bactericidal, and Biocompatible Surface, *ACS Appl. Mater. Interfaces*. 9 (2017) 24381–24392. doi:10.1021/acsami.7b08368.
- [5] S. Peng, B. Bhushan, Mechanically durable superoleophobic aluminum surfaces with microstep and nanoreticula hierarchical structure for self-cleaning and anti-smudge properties, *J. Colloid Interface Sci.* 461 (2016) 273–284. doi:10.1016/j.jcis.2015.09.027.
- [6] G. McHale, M.I. Newton, N.J. Shirtcliffe, Immersed superhydrophobic surfaces: Gas exchange, slip and drag reduction properties, *Soft Matter*. 6 (2010) 714–719. doi:10.1039/b917861a.
- [7] J. Brassard, J. Laforte, C. Blackburn, J. Perron, D.K. Sarkar, Silicone based superhydrophobic coating efficient to reduce ice adhesion and accumulation on aluminum under offshore arctic conditions, *Ocean Eng.* 144 (2017) 135–141. doi:10.1016/J.OCEANENG.2017.08.022.
- [8] R.N. Wenzel, Resistance of solid surfaces to wetting by water, *Ind. Eng. Chem.* 28 (1936) 988–994. doi:10.1021/ie50320a024.
- [9] A.B.D. Cassie, S. Baxter, Wettability of porous surfaces, *Physics (College. Park. Md)*. (1944) 546–551. doi:10.1039/tf9444000546.
- [10] M. Liu, S. Wang, L. Jiang, Nature-inspired superwettability systems, *Nat. Rev. Mater.* 2 (2017). doi:10.1038/natrevmats.2017.36.
- [11] B. Su, Y. Tian, L. Jiang, Bioinspired Interfaces with Superwettability: From Materials to Chemistry, *J. Am. Chem. Soc.* 138 (2016) 1727–1748. doi:10.1021/jacs.5b12728.
- [12] Z. Wang, M. Elimelech, S. Lin, Environmental Applications of Interfacial Materials with Special Wettability, *Environ. Sci. Technol.* 50 (2016) 2132–2150. doi:10.1021/acs.est.5b04351.
- [13] X. Zhou, Z. Zhang, X. Xu, F. Guo, X. Zhu, X. Men, B. Ge, Robust and durable superhydrophobic cotton fabrics for oil/water separation, *ACS Appl. Mater. Interfaces*. 5 (2013) 7208–7214. doi:10.1021/am4015346.
- [14] H. Liu, Y. Kang, Superhydrophobic and superoleophilic modified EPDM foam rubber fabricated by a facile approach for oil/water separation, *Appl. Surf. Sci.* 451 (2018) 223–231. doi:10.1016/j.apsusc.2018.04.179.
- [15] J. Li, X. Bai, X. Tang, F. Zha, H. Feng, W. Qi, Underwater superoleophobic/underoil superhydrophobic corn cob coated meshes for on-demand oil/water separation, *Sep. Purif. Technol.* 195 (2018) 232–237. doi:10.1016/j.seppur.2017.12.023.

- [16] N. Cao, B. Yang, A. Barras, S. Szunerits, R. Boukherroub, Polyurethane sponge functionalized with superhydrophobic nanodiamond particles for efficient oil/water separation, *Chem. Eng. J.* 307 (2017) 319–325. doi:10.1016/j.cej.2016.08.105.
- [17] I. Vilaró, J.L. Yagüe, S. Borrós, Superhydrophobic Copper Surfaces with Anticorrosion Properties Fabricated by Solventless CVD Methods, *ACS Appl. Mater. Interfaces.* 9 (2017) 1057–1065. doi:10.1021/acsami.6b12119.
- [18] S.D. Bhagat, M.C. Gupta, Superhydrophobic microtextured polycarbonate surfaces, *Surf. Coatings Technol.* 270 (2015) 117–122. doi:10.1016/j.surfcoat.2015.03.013.
- [19] F.J.M. Ruiz-Cabello, P.F. Ibáñez-Ibáñez, J.F. Gómez-Lopera, J. Martínez-Aroza, M. Cabrerizo-Vílchez, M.A. Rodríguez-Valverde, Testing the performance of superhydrophobic aluminum surfaces, *J. Colloid Interface Sci.* 508 (2017) 129–136. doi:10.1016/j.jcis.2017.08.032.
- [20] A.M. Escobar, N. Llorca-Isern, Superhydrophobic coating deposited directly on aluminum, *Appl. Surf. Sci.* 305 (2014) 774–782. doi:10.1016/j.apsusc.2014.03.196.
- [21] Z. Wei, D. Jiang, J. Chen, X. Guo, Combination of chemical etching and electrophoretic deposition for the fabrication of multi-scale superhydrophobic Al films, *Mater. Lett.* 196 (2017) 115–118. doi:10.1016/j.matlet.2017.03.024.
- [22] J. Xiong, D.K. Sarkar, X.G. Chen, Superhydrophobic honeycomb-like cobalt stearate thin films on aluminum with excellent anti-corrosion properties, *Appl. Surf. Sci.* 407 (2017) 361–370. doi:10.1016/j.apsusc.2017.02.203.
- [23] A.M. Escobar, N. Llorca-Isern, O. Rius-Ayra, Identification of the mechanism that confers superhydrophobicity on 316L stainless steel, *Mater. Charact.* 111 (2016) 162–169. doi:10.1016/j.matchar.2015.11.026.
- [24] N. Llorca-Isern, A.M. Escobar, O. Rius, Scalable Methods to Obtain Superhydrophobicity onto Metallic Surface, *Mater. Sci. Forum.* 879 (2016) 2501–2506. doi:10.4028/www.scientific.net/MSF.879.2501.
- [25] G. Wang, S. Liu, S. Wei, Y. Liu, J. Lian, Q. Jiang, Robust superhydrophobic surface on Al substrate with durability, corrosion resistance and ice-phobicity, *Sci. Rep.* 6 (2016) 20933. doi:10.1038/srep20933.
- [26] A. Sadeghi, M. Sieber, I. Scharf, T. Lampke, Co-deposition behavior of alumina nanoparticles and properties of Ni-Al₂O₃, *Surf. Interface Anal.* 47 (2015) 738–744. doi:10.1002/sia.5771.

- [27] M.H. Allahyarzadeh, M. Aliofkhazraei, A.R.S. Rouhaghdam, V. Torabinejad, Electrodeposition of Ni-Fe and Ni-Fe-(nano Al₂O₃) multilayer coatings, *J. Alloys Compd.* 666 (2016) 217–226. doi:10.1016/j.jallcom.2016.01.031.
- [28] I. Corni, R.J. Chater, A.R. Boccaccini, M.P. Ryan, Electro co-deposition of Ni-Al₂O₃ composite coatings, *J. Mater. Sci.* 47 (2012) 5361–5373. doi:10.1007/s10853-012-6381-7.
- [29] S. Karthikeyan, L. Vijayaraghavan, S. Madhavan, A. Almeida, Study on the Mechanical Properties of Heat-Treated Electroless NiP Coatings Reinforced with Al₂O₃ Nano Particles, *Metall. Mater. Trans. A Phys. Metall. Mater. Sci.* 47 (2016) 2223–2231. doi:10.1007/s11661-016-3413-y.
- [30] D. Iacovetta, J. Tam, U. Erb, Synthesis, structure, and properties of superhydrophobic nickel-PTFE nanocomposite coatings made by electrodeposition, *Surf. Coatings Technol.* 279 (2015) 134–141. doi:10.1016/j.surfcoat.2015.08.022.
- [31] L. Chen, L. Wang, Z. Zeng, J. Zhang, Effect of graphite concentration on the friction and wear of Ni–Al₂O₃/graphite composite coatings by a combination of electrophoresis and electrodeposition, *Wear.* 434 (2006) 319–325. doi:10.1016/j.msea.2006.06.098.
- [32] S. Men, X. Jiang, X. Xiang, G. Sun, Y. Yan, Z. Lyu, Y. Jin, Synthesis of Cellulose Long-Chain Esters in 1-Butyl-3-methylimidazolium Acetate: Structure-Property Relations, *Polym. Sci. - Ser. B.* 60 (2018) 349–353. doi:10.1134/S1560090418030144.
- [33] Q. Xu, S. Hu, W. Wang, Y. Wang, H. Ju, J. Zhu, Temperature-induced structural evolution of Sm nanoparticles on Al₂O₃ thin film: An in-situ investigation using SRPES, XPS and STM, *Appl. Surf. Sci.* (2016) 1–6. doi:10.1016/j.apsusc.2016.11.145.
- [34] P. Gautier, A. Vallee, C. Sinito, A. Etcheberry, N. Simon, Effect of growth temperature on the electrodeposition of zinc oxide layers on diamond surfaces, *Diam. Relat. Mater.* 62 (2016) 1–6. doi:10.1016/j.diamond.2015.12.005.
- [35] T. Liu, X. Fei, L. Hu, H. Zhang, Y. Li, S. Duo, Effect of substrate surface pretreatment and annealing treatment on morphology, structure, optical and electrical properties of sputtered ZnO films, *Superlattices Microstruct.* 83 (2015) 604–617. doi:10.1016/j.spmi.2015.04.007.
- [36] M. Gadermann, T.C. Preston, C. Troster, R. Signorell, Characterization of palmitic and lauric acid aerosols from rapid expansion of supercritical CO₂ solutions, *Mol. Phys.* 106 (2008) 945–953. doi:10.1080/00268970802020355.

- [37] M.L. Caroline, S. Vasudevan, Growth and characterization of an organic nonlinear optical material-lauric acid crystal, *Mater. Res. Express.* 62 (2008) 2245–2248. doi:10.1016/j.matlet.2007.11.059.
- [38] L. Jiesheng, Y. Yuanyuan, H. Xiang, Research on the preparation and properties of lauric acid/expanded perlite phase change materials, *Energy Build.* 110 (2016) 108–111. doi:10.1016/j.enbuild.2015.10.043.
- [39] K. Rajeswari, K. Pandiarajan, Powder X-ray diffraction, infrared and ¹³C NMR spectroscopic studies of the homologous series of some solid-state zinc(II) and sodium(I) n-alkanoates, *Spectrochim. Acta Part A Mol. Biomol. Spectrosc.* 78 (2010) 1110–1118. doi:10.1016/j.saa.2010.12.062.
- [40] M. Estruga, C. Domingo, J.A. Ayllón, Solution-processable ZnO nanoparticles obtained by low-temperature solventless synthesis, *J. Mater. Chem.* 21 (2011) 4408. doi:10.1039/c0jm03812a.
- [41] J.J. Hermans, K. Keune, A. van Loon, P.D. Iedema, An infrared spectroscopic study of the nature of zinc carboxylates in oil paintings, *J. Anal. At. Spectrom.* 30 (2015) 1600–1608. doi:10.1039/C5JA00120J.
- [42] C. Liu, K. Shih, Y. Gao, F. Li, L. Wei, Dechlorinating transformation of propachlor through nucleophilic substitution by dithionite on the surface of alumina, *J. Soils Sediments.* 12 (2012) 724–733. doi:10.1007/s11368-012-0506-0.
- [43] X. Tian, T. Verho, R.H.A. Ras, Moving superhydrophobic surfaces toward real-world applications., *Science.* 352 (2016) 142–3. doi:10.1126/science.aaf2073.
- [44] H. Jin, X. Tian, O. Ikkala, R.H.A. Ras, Preservation of superhydrophobic and superoleophobic properties upon wear damage, *ACS Appl. Mater. Interfaces.* 5 (2013) 485–488. doi:10.1021/am302541f.
- [45] V. Jokinen, P. Suvanto, A.R. Garapaty, J. Lyytinen, J. Koskinen, S. Franssila, Durable superhydrophobicity in embossed CYTOP fluoropolymer micro and nanostructures, *Colloids Surfaces A Physicochem. Eng. Asp.* 434 (2013) 207–212. doi:10.1016/j.colsurfa.2013.05.061.
- [46] L. Xu, D. Zhu, X. Lu, Q. Lu, Transparent, thermally and mechanically stable superhydrophobic coating prepared by an electrochemical template strategy, *J. Mater. Chem. A.* 3 (2015) 3801–3807. doi:10.1039/C4TA06944G.
- [47] L.R.J. Scarratt, U. Steiner, C. Neto, A review on the mechanical and thermodynamic robustness of superhydrophobic surfaces, *Adv. Colloid Interface Sci.* 246 (2017) 133–152. doi:10.1016/j.cis.2017.05.018.
- [48] A. Milionis, E. Loth, I.S. Bayer, Recent advances in the mechanical durability of superhydrophobic materials, *Adv. Colloid Interface Sci.* 229 (2016) 57–79. doi:10.1016/j.cis.2015.12.007.

- [49] Z. Cheng, J. Wang, H. Lai, Y. Du, R. Hou, C. Li, N. Zhang, K. Sun, pH-Controllable On-Demand Oil/Water Separation on the Switchable Superhydrophobic/Superhydrophilic and Underwater Low-Adhesive Superoleophobic Copper Mesh Film, *Langmuir*. 31 (2015) 1393–1399. doi:10.1021/la503676a.
- [50] X. Yue, T. Zhang, D. Yang, F. Qiu, Z. Li, Hybrid aerogels derived from banana peel and waste paper for efficient oil absorption and emulsion separation, *J. Clean. Prod.* 199 (2018) 411–419. doi:10.1016/j.jclepro.2018.07.181.
- [51] T. Yuan, J. Meng, T. Hao, Z. Wang, Y. Zhang, A Scalable Method toward Superhydrophilic and Underwater Superoleophobic PVDF Membranes for Effective Oil / Water Emulsion Separation, *ACS Appl. Mater. Interfaces*. 7 (2015) 14896–14904. doi:10.1021/acsami.5b03625.
- [52] X. Di, W. Zhang, Z. Jiang, M. Zhang, Y. Wang, F. Liu, S.-H. Ho, C. Wang, Facile and rapid separation of oil from emulsions by hydrophobic and lipophilic Fe₃O₄/sawdust composites, *Chem. Eng. Res. Des.* 129 (2018) 102–110. doi:10.1016/j.cherd.2017.10.025.
- [53] J. Gu, P. Xiao, J. Chen, F. Liu, Y. Huang, G. Li, J. Zhang, T. Chen, Robust preparation of superhydrophobic polymer/carbon nanotube hybrid membranes for highly effective removal of oils and separation of water-in-oil emulsions, *J. Mater. Chem. A*. 2 (2014) 15268–15272. doi:10.1039/c4ta01603c.